Hindawi
Shock and Vibration
Volume 2021, Article ID 1869583, 16 pages
https://doi.org/10.1155/2021/1869583

Research Article

Numerical Simulation of Mechanical Characteristics of Roadway Surrounding Rock under Dynamic and Static Loading

Ce Jia, Sheng Li, Chaojun Fan, and Jinbao Tang

College of Mining, Liaoning Technical University, Fuxin 12300, China

Correspondence should be addressed to Sheng Li; 13941811946@139.com

Received 6 October 2021; Accepted 2 November 2021; Published 23 December 2021

Academic Editor: Xuesheng Liu

Mechanical characteristics of roadway surrounding rock under different stress wave disturbances are the key to design roadway supporting scheme. In this study, the 2802 transportation roadway in Zhangcun Coal Mine is selected as the engineering background. The distribution of stress, displacement, and plastic zone in surrounding rock under the impact of different stress waves is studied. Results show that the stress and displacement of the roof, floor, and coal walls present fluctuating change with time during the stress wave loading process. With the increase of disturbing intensity of stress wave, the resistance ability for stress wave disturbance of the roof is lower than that of the floor, while the resistance ability of two sides is the same. The volume of plastic zone in roadway surrounding rock was calculated by the self-compiled FISH code. The relationship between the plastic zone volume and the stress wave disturbing intensity in different states is explored. The cubic polynomial relationship between the volume and the disturbing intensity in the state of shear_past and tension_past is obtained. Under the simulated condition, the disturbing intensity of stress wave has the greatest influence on the increase of shear_past volume when it equals 11 MPa. While the disturbing intensity of stress wave has the greatest influence on the increase of tension_past volume, it equals 7 MPa. Meanwhile, the relation between stress wave disturbing intensity and surrounding rock stress and displacement is obtained respectively. The achievements provide a theoretical base for roadway surrounding rock support under dynamic and static loading.

1. Introduction

With the increase of the scope and depth of coal mining, China's coal mining has gradually entered the deep mining stage [1]. The current mining depth in China has reached 1500 m [2, 3]. During coal mining, a series of safety problems caused by the large deformation and destruction of surrounding rock of deep buried roadway need to be further solved [4]. The mining process inevitably bears the stress adjustment disturbance caused by the machinery or blasting induced loading/unloading. It belongs to the typical dynamic and static combined stress state [5]. Therefore, a better understanding of the mechanical properties of roadway surrounding rock under the action of dynamic and static combined loading is beneficial to improve the stability of surrounding rock and provide reference for the optimization of support design.

The methods of experimental testing and numerical simulation are carried out to study the deformation and failure behaviors of roadway surrounding rock under dynamic and static combined loading. Wang et al. [6] developed a test equipment to study the damage of the surrounding rock of the roadway by dynamic loading. When roadway surrounding rock reaches its bearing capacity, this increases the input energy of the dynamic load and increases the AE events and causes serious damage to the surrounding rock. Other test experiments were conducted. Guo et al. [7] used the digital laser dynamic caustics system to study the influence of the blasting load on the adjacent roadway. Tang et al. [8] used the SHBP experimental device to simulate the dynamic mechanical response and energy dissipation behavior of coal samples under impact loads. The main methods of numerical simulation include discrete element method, analytical method, and finite element method

[9–17]. Qian et al. [17–20] simulated and studied the influence of lateral pressure coefficient, dynamic load amplitude, and disturbance time on the stability of roadway surrounding rock by using software of RFPA, PFC^{2D}, and FLAC^{3D}. They pointed out that with the increase of dynamic load amplitude and disturbance time, the deformation of roadway surrounding rock increases, as well as the stress, displacement, and the number of cracks on the roof and floor. As a result, the damage degree of roadway increases and the stability becomes worse. Fan et al. [21] simulated the response characteristics of the surrounding rock of deep chamber with a large section under the influence of dynamic and static loads by the dynamic module of FLAC^{3D}. The stress, deformation, and rupture range of surrounding rock under static load were analyzed, as well as the response law of chamber surrounding rock under different frequency, intensity of impact loadings, and distance between chambers. Wang et al. [22] simulated the mechanical response of roadway surrounding rock under dynamic disturbance. The greater the original rock stress, the more significant the impact of dynamic disturbance on roadway surrounding rock. For deep high-stress roadways, the dynamic disturbance causes peak horizontal stress in roof and floor and reaches a very high stress state to form a large-scale plastic yield area with a risk of rock burst. Jia et al. [23] studied the nonlinear evolution characteristics of surrounding rock and discussed the influence of mining sequence on its stability by three-dimensional dynamic finite difference method. Kong et al. [24] investigated the deformation of roadway under different dynamic and static loadings using fast Lagrangian analysis software. It is found that the greater the dynamic load, the greater the increase in roadway deformation under the same static loading. Under different static loadings, the dynamic response of the stress distribution of roadway surrounding rock is different. Xue et al. [25] simulated the damage of dynamic stress to roadway surrounding rock by using UDEC software and explored the influence of the thickness and strength of the roof. The above research reveals the deformation and failure laws of roadway surrounding rock under the action of dynamic and static combined loadings from different points of view.

However, the studying of influencing factors on the stability of surrounding rock is limited as only one factor is considered at the same time. In the deep mining, the dynamic damage and deformation of surrounding rock are resulted by a combination of multiple factors. This paper designs 7 sets of plans and uses FLAC^{3D} software to study the stress, displacement, and plastic zone distribution of roadway surrounding rock under different stress wave disturbance intensities. The functional relationship between the volume of plastic zone and the intensity of stress wave in different states is obtained. The changes of displacement, stress, and plastic zone of roadway surrounding rock are analyzed. The polynomial function of the maximum stress and displacement in the roof, floor, and two sides of roadway and the intensity of stress wave are fitted. The results provide a theoretical guidance for roadway surrounding rock control under dynamic and static loading.

2. Failure Mechanism of Roadway Surrounding Rock under Dynamic and Static Loading

During underground mining, dynamic phenomenon such as roof failure, fault activation, rock burst, and coal and gas outburst occur usually accompanying stress waves. The stress wave generates an impact loading in the rock mass and subsequently propagates outward as shown in Figure 1. When the stress wave encounters the interface between two types of media, part of the stress wave is transmitted or refracted through the interface, and the rest part of stress wave is reflected. The refraction, reflection, and transmission of stress waves are related to the impedance characteristics of the media on both sides of the interface, which are reflected by the wave impedance function of each dielectric layer in dynamic impact. According to the theory of continuum mechanics, the excavation of roadway will cause redistribution of surrounding stress [26]. When the stress wave generated by the fault slip vibration propagates in the infinite and uniform ideal surrounding rock, it transports in all directions with the wave source as the center. The impact loading is generated during the wave propagation process, which causes roadway surrounding rock to form different areas in coal and rock with different stress and deformation states, namely, the broken, plastic, and elastic zones.

Assuming that coal and rock medium is isotropic and continuous, the impact loading generated by the longitudinal wave (P wave) in the medium is derived based on the elastic wave theory [27]:

$$\sigma_{dp} = \rho c_p v_p, \tag{1}$$

where σdp is the dynamic load generated by the P wave, Pa; ρ is the medium density, kg/m^3; c_p is the P wave propagation velocity, m/s; and v_p is the peak vibration velocity caused by the P wave, m/s.

Another basic wave generated by vibration is transverse wave (S wave). The direction of particle vibration caused by transverse wave is perpendicular to the direction of propagation. The propagation of transverse wave generates shear stress in coal and rock medium. The impact loading on coal and rock medium caused by transverse wave propagation is [22]

$$\sigma_{ds} = G\gamma, \tag{2}$$

where G is the shear modulus, MPa, and γ is the shear strain.

During the time period of dt, the tangent of the tangential angle variable θ of coal and rock media caused by shear waves is defined as

$$\begin{aligned} \tan\,\theta &= \frac{v_s \mathrm{d}t}{c_s \mathrm{d}t} \\ &= \frac{v_s}{c_s}, \end{aligned} \tag{3}$$

where c_s is the propagation velocity of transverse wave, m/s, and vs is the maximum vibration velocity caused by the propagation of transverse wave, m/s.

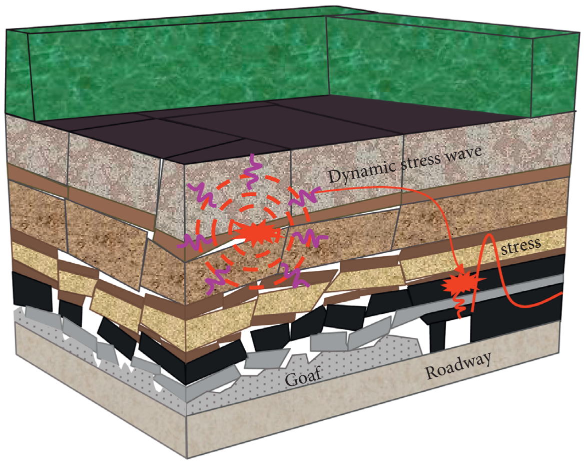

Figure 1: Failure mechanism of roadway surrounding rock under impact loading.

Because the medium vibration velocity is far lower than the shear wave velocity,

$$\gamma = \tan\,\theta = \frac{v_s dt}{c_s st} = \frac{v_s}{c_s}. \tag{4}$$

From the elastic wave theory,

$$c_s = \sqrt{\frac{G}{\rho}}. \tag{5}$$

From (2) and (4), and (5), the impact loading generated by the transverse wave can be solved as

$$\sigma_s = \rho c_s v_s. \tag{6}$$

The impact loading generated by stress wave is

$$\begin{cases} \sigma_{dp} = \rho c_s v_p, \\ \sigma_{ds} = \rho c_s v_s. \end{cases} \tag{7}$$

The stress in coal and rock mass is in equilibrium at beginning if there is no mining disturbance [28]. The equilibrium broken by the mining will cause energy release. When the released energy is greater than the consumed energy, the redundant energy will lead to dynamic damage. The expression can be described as [29]

$$\frac{\mathrm{d}U_R}{\mathrm{d}t} + \frac{\mathrm{d}U_c}{\mathrm{d}t} + \frac{\mathrm{d}U_s}{\mathrm{d}t} > \frac{\mathrm{d}U_B}{\mathrm{d}t}, \tag{8}$$

where *UR* is the energy stored in the surrounding rock, J; *UC* is the energy stored in the coal, J; *US* is the energy input by the mine earthquake, J; and *UB* is the energy consumed by the coal and rock when the rock burst occurs, J. The sum of the energy stored in coal and rock mass and the energy stem from the stress wave can be expressed as

$$U = \frac{(\sigma_s + \sigma_d)^2}{2E}, \tag{9}$$

$$U_{b\min} = \frac{\sigma_{b\min}^2}{2E}, \tag{10}$$

where *σs* is the static load of coal and rock mass, Pa; *σd* is the dynamic load of coal and rock mass, Pa; *σbmin* is the critical impact loading, MPa; *U* is the sum of the energy stored in coal and rock mass and the energy stem from the stress wave, J; *Ubmin* is the critical minimum energy for impact, J; and *E* is elastic modulus.

According to (8) and (9), and (10), the conditions of the shock manifestation stress can be obtained, namely,

$$\sigma_s + \sigma_d, \quad \geq \sigma_{b\min}. \tag{11}$$

When the impact loading and the static loading superimpose and exceed the critical strength of surrounding rock, the dynamic phenomenon will occur, and the roadway surrounding rock will be destroyed and deformed.

3. Calculation Model and Plan

3.1. Engineering Geological Background. The 2802 transportation roadway studied in this paper is located in the No. 3 coal seam in Zhangcun Coal Mine, Shanxi Province. The coal seam is stable with an average thickness of 6.03 m. The geological histogram is shown in Figure 2. The 2802 transportation roadway is arranged along the floor, with a design length of 2050 m. The section of roadway is rectangular, with the tunneling section area of 18.9 m^2. The 2802 transportation roadway is excavated in coal seam, which is prone to be damaged under the disturbance of high stress or dynamic loading.

3.2. Schedule for Static Analysis. According to the geological conditions of 2802 haulage roadway, the calculation model is established to study the mechanical characteristics and instability deformation process of the roadway surrounding rock under different stress wave intensities by the dynamics module of FLAC3D software. Assuming that the model is isotropic, the Mohr Coulomb criterion is used for simulation. The specific parameters used in the simulation process are shown in Table 1. The model size is 40 m × 10 m × 20.56 m (length × width × height). The geometry model is divided into 69000 elements. The roadway is tunneled along the 3# coal floor, the section is rectangular, the size is 5.4 × 4.0 m (width × height), and the overall model is shown in Figure 3.

Before dynamic calculation, static balance is first performed. In the static calculation, roller constraint is applied on the left and right boundaries of the model, while the fixed condition is for floor boundary, and uniformly distributed loading condition with the weight of the overlying rock is for the upper boundary. The static calculation model is shown in Figure 4. The roof of the model is buried at a depth of 400 m, and the upper boundary loading is 10 MPa.

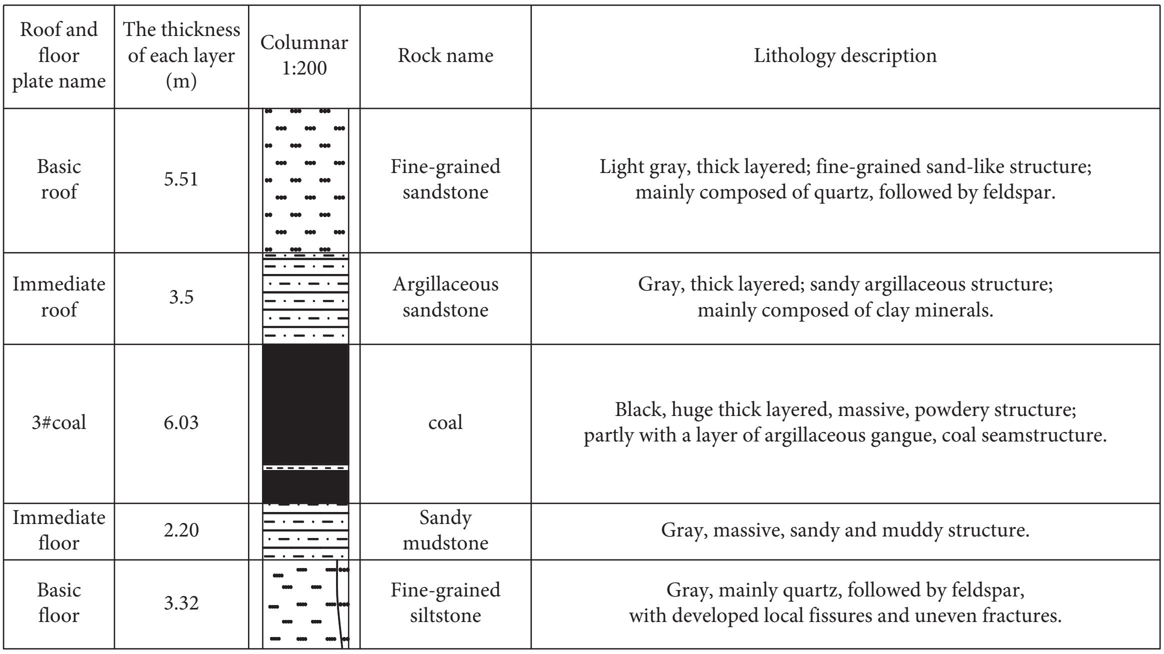

Roof and floor plate name	The thickness of each layer (m)	Columnar 1:200	Rock name	Lithology description
Basic roof	5.51		Fine-grained sandstone	Light gray, thick layered; fine-grained sand-like structure; mainly composed of quartz, followed by feldspar.
Immediate roof	3.5		Argillaceous sandstone	Gray, thick layered; sandy argillaceous structure; mainly composed of clay minerals.
3#coal	6.03		coal	Black, huge thick layered, massive, powdery structure; partly with a layer of argillaceous gangue, coal seamstructure.
Immediate floor	2.20		Sandy mudstone	Gray, massive, sandy and muddy structure.
Basic floor	3.32		Fine-grained siltstone	Gray, mainly quartz, followed by feldspar, with developed local fissures and uneven fractures.

Figure 2: Geological histogram.

Table 1: Rock mechanics parameter.

Roof and floor plate name	Bulk density (kg/cm^3)	Bulk modulus (GPa)	Shear modulus (GPa)	Cohesion (MPa)	Internal friction angle (°)	Tensile strength (MPa)	Remark
Basic roof	2873	21.01	13.5	3.2	42	1.29	Experiments
Immediate roof	2487	5.97	6.01	2.06	40	1.13	Experiments
3#coal	1380	4.91	2.01	1.25	32	0.15	Experiments
Immediate floor	2483	9.97	7.35	1.2	32	0.58	Experiments
Basic floor	2460	10.83	8.13	3.75	38	1.84	Experiments

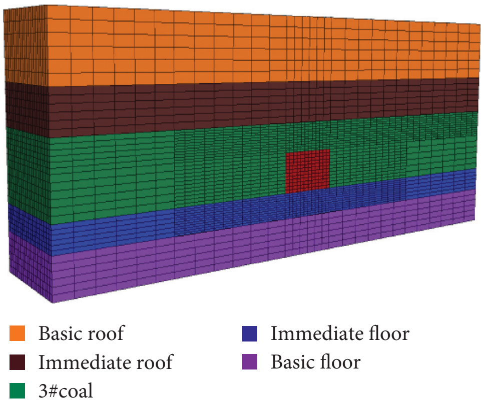

Figure 3: Meshing of the 3D model.

3.3. Schedule for Dynamic Analysis. In the mining operations, the disturbing stress produced by the failure of key strata, fault slip, blasting, and seismic vibration can be loaded in the form of stress wave. Complex shock waves can be filtered through Fourier algorithm for high frequency and low frequency waves and replaced by simple harmonics. Sun et al. [30] simplified the impact loading to be a half sine wave and compiled it in fish language to embed it in the dynamic calculation process. The stress-time curve is shown in Figure 5:

$$F = \begin{cases} \sigma\left(1 - \cos\left(2\pi f t\right)\right), & \dfrac{t < 1}{f}, \\[2ex] 0, & \dfrac{t > 1}{f}, \end{cases} \tag{12}$$

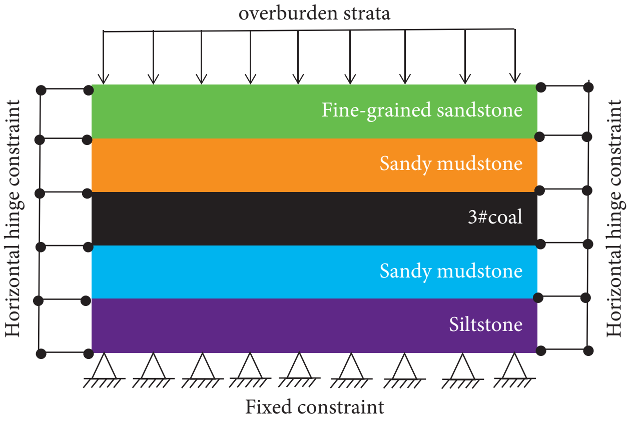

FIGURE 4: Boundary condition of the static calculation model.

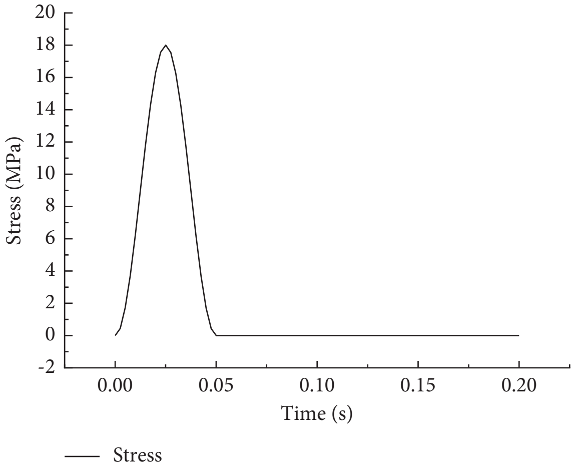

FIGURE 5: Variation of disturbing stress wave with time.

where σ is the peak stress, MPa; f is the disturbance frequency, Hz; and t is the dynamic load loading time, s.

According to the in-situ observation in literature [31], the frequency of stress wave is mainly concentrated within 0–50 Hz. In this paper, the frequency of the stress wave is set to 20 Hz, and the stress wave loading time is 0.2 s. Seven calculation schemes are designed to compare and analyze the mechanical characteristics of roadway surrounding rock under different stress wave intensities. The peak stresses of Scheme 1 to Scheme 7 are 3, 5, 7, 9, 11, 13, and 15 MPa, respectively. This paper adopts the value range of peak stress in the literature [32] and refers to the microseismic monitoring data in field.

After the static force is balanced, the dynamic calculation is performed. An impact loading is applied to the upper boundary to simulate the impact loading caused by the slippage of fault during the mining process. FLAC3D software provides two types of damping, namely local damping and Rayleigh damping. According to literature [33], Rayleigh damping is selected, with a minimum damping ratio of 0.3% and a center frequency of 5.2 Hz. The static viscous boundary condition is used to reduce the stress wave reflection, and the nonreflective boundary is used on the top boundary of the model. Since the model is taken from the deep semi-infinite boundary of rock mass, nonreflective boundaries are used on both sides and bottom of the model to absorb normal incident waves. The dynamic calculation model is shown in Figure 6.

3.4. Procedure of Numerical Simulations. Step 1: before excavation, balance the ground stress in the model until reaching the static equilibrium. Step 2: excavate the roadway with size 5.4 × 4.0 m (width × height) until the model is in static equilibrium (step = 10654). Step 3: before dynamics calculation, arrange monitoring points on the roof, floor, and two sides of roadway surrounding rock to monitor changes in stress and displacement. Step 4: apply a vertical downward half-sine compressive stress wave on the top of the model and continue the calculation. When step = 110654, the first compressive stress wave is transmitted into the model. The detailed steps are shown in Figure 7.

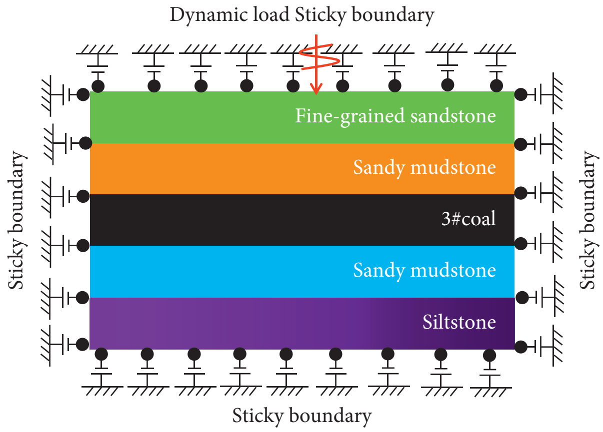

Figure 6: Boundary condition of the dynamic calculation model.

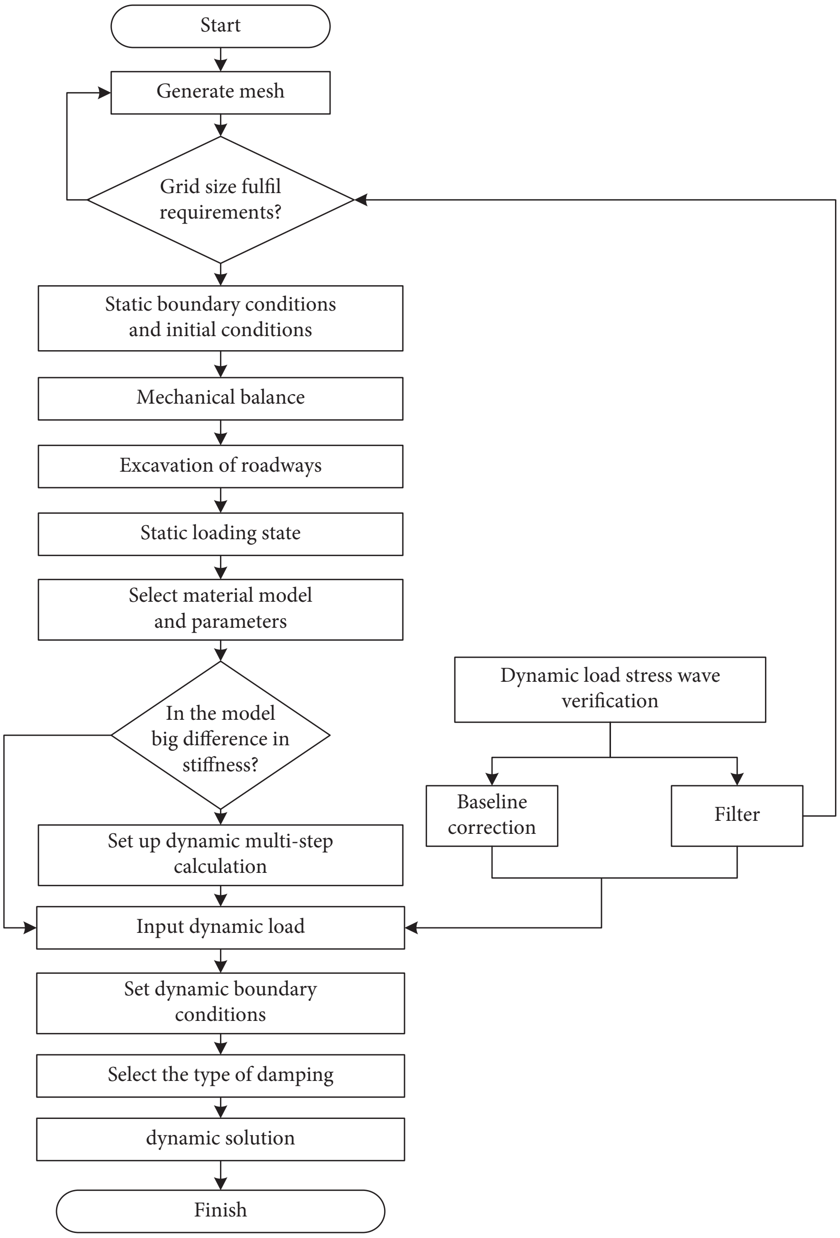

Figure 7: Simulation flow chart.

4. Results and Discussion on Numerical Simulations

4.1. Stress Evolution in Surrounding Rocks. Figure 8 shows the relationship between vertical stress of roadway surrounding rock and the intensity of stress wave disturbance. In Figures 8(a)–8(d), when the disturbing intensity of stress wave increases from 0 MPa to 15 MPa, the stress concentration area in the roof and floor of roadway increases, and the stress concentration area of two sides decreases. With the increase of disturbing intensity, the stress concentration area of roof and floor increases. The stress concentration also intensified, leading to an increase in the damage range of the surrounding rock. The location of the peak stress concentration shifts toward the deep surrounding rock. Under the influence of stress wave disturbance, the stress concentration area in roof and floor is larger than that in two sides. Meanwhile, the damage in roof and floor is more serious.

Figure 9 presents the relationship between the horizontal stress of roadway surrounding rock and the disturbing intensity of stress wave. In Figures 9(a)–9(d), when the intensity of stress wave disturbance increases from 0 MPa to 15 MPa, the stress concentration area in roof and floor of roadway increases. The increase in the stress concentration area in two sides is greater than that in roof and floor. The bearing capacity and stress of roadway surrounding rock determine the elastoplastic deformation state. The deformation and failure of surrounding rock in turn affect the bearing capacity and stress, until the surrounding rock reaches a mechanical equilibrium state. The stress wave forms an impact loading during the propagation in coal and rock mass. As the stress peak increases, the generated dynamic load gradually increases, resulting in obvious regional division of the stress in surrounding rock.

Figure 10 illustrates the time history curve of the vertical stress in roof and floor of roadway and the horizontal stress in two sides. The disturbing time of stress wave is 0.1 s. In Figures 10(a)-10(b), when the disturbing intensity of stress wave increases, the stress in roof and floor shows an increase-decrease-stabilize trend. As shown in Figure 10(a), when the time is from 0.01 s to 0.05 s, the stress is negative, and the pressure is compressive stress. At time of 0.05 s, the entire stress wave enters the surrounding rock. After 0.05 s, the roof stress is all positive, and tensile stress appears. The tensile strength of the rock medium is far lower than its compressive strength. When tensile stress and compressive stress alternately act, the deformation in the roof and floor accumulates, which provides the possibility of outburst failure for the internal rock mass. As shown in Figure 10(b), the stress value is positive between 0.01 s and 0.05 s, and tensile stress appears. The reflection and transmission of stress waves appear on the free surface. Because the surrounding rock has the effect of medium damping, the stress wave will be consumed during the propagation process, and the vertical stress in roof and floor will gradually decrease and tend to be static load.

Figure 11 shows the relationship between the maximum, minimum, and stable vertical stress in roof and floor, the horizontal stress of two sides, and the disturbing intensity of stress wave. When the intensity of the stress wave increases, the stresses in surrounding rock increase. The minimum stress in roof is similar with that of stable stress. The quadratic interpolation polynomial function between the maximum stress in roof and the intensity of stress wave is shown in Figure 11(a). In Figure 11(b), the increase amplitude in the stable stress is the largest. The cubic interpolation polynomial function is fitted between the maximum stress in floor and the intensity of stress wave. The disturbance of stress wave has a great influence on the maximum stress in roof and the stable stress in floor. From Figures 11(c)–11(d), the stresses of two sides are similar. When the disturbing intensity equals 9 MPa, the stable value of stress is close to the minimum value. When intensity is smaller than 9 MPa, the stable value is greater than the minimum value. When the intensity is greater than 9 MPa, the minimum value is greater than the stable value. The cubic interpolation polynomial function is fitted between the disturbing intensity of stress wave and stress in two sides.

4.2. Displacement Evolution in Surrounding Rocks. Figure 12 shows the relationship between vertical displacement of roadway surrounding rock and the disturbing intensity of stress wave. From Figure 12(a), when the disturbing intensity of stress wave is 0 MPa, the roof sinks and the floor heaves. As shown in Figure 12(b), when the disturbing intensity of stress wave is 5 MPa, the maximum roof subsidence increases about 1.7 mm, and the floor displacement appears negative. In Figure 12(c), the maximum roof subsidence increases, the influence range decreases, and the subsidence around the roadway increases. The influence range of roof subsidence in Figure 12(d) is larger than that in Figure 12(c), while the maximum subsidence amount increases about 17 mm. From Figures 12(a)–12(d), when the disturbing intensity of stress wave increases, the influence range of roof and floor displacement extends. The disturbance of stress wave has great influence on roof subsidence. When the propagation of stress wave encounters a free surface, the negative displacement in floor will be resulted.

Figure 13 presents the evolution of vertical displacement in roof and floor and horizontal displacement of two sides of the roadway. From Figure 13(a), when the disturbing intensity of stress wave is 0 MPa, the influencing range of the displacement is larger in two sides of the roadway. In Figures 13(b)–13(d), when the disturbing intensity of stress wave increases, the displacement increasing area on the two sides of roadway extends and the maximum displacement increases. Figures 13(b)–13(d) illustrate that the maximum displacement of the right side has increased from 4.84 mm to 26.6 mm, with a growth rate of 449.5%. The maximum displacement of the left side increases from 4.85 mm to 26.6 mm, and the growth rate reaches 448.4%. Under the action of stress wave disturbance, the resistance ability of stress wave disturbance in two sides of roadway surrounding rock is similar.

Figure 14 illustrates the evolution of vertical displacement in roof and floor of roadway and horizontal

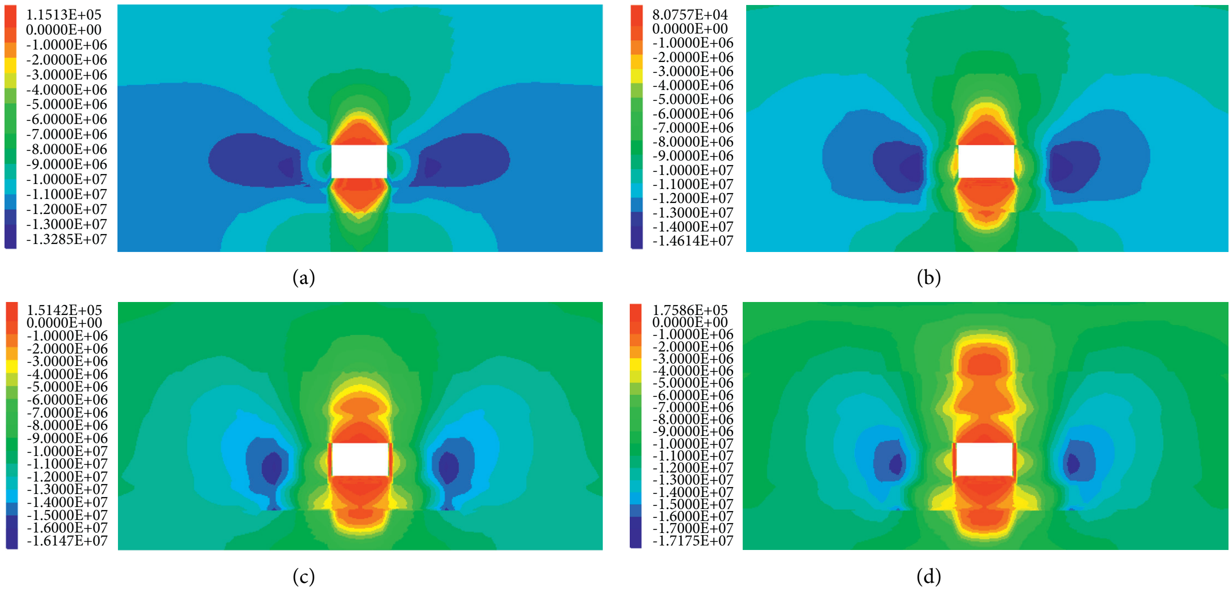

FIGURE 8: Vertical stress cloud diagram. (a) Vertical stress with peak stress wave of 0 MPa. (b) Vertical stress with peak stress wave of 0 MPa. (c) Vertical stress with peak stress wave of 11 MPa. (d) Vertical stress with peak stress wave of 15 MPa.

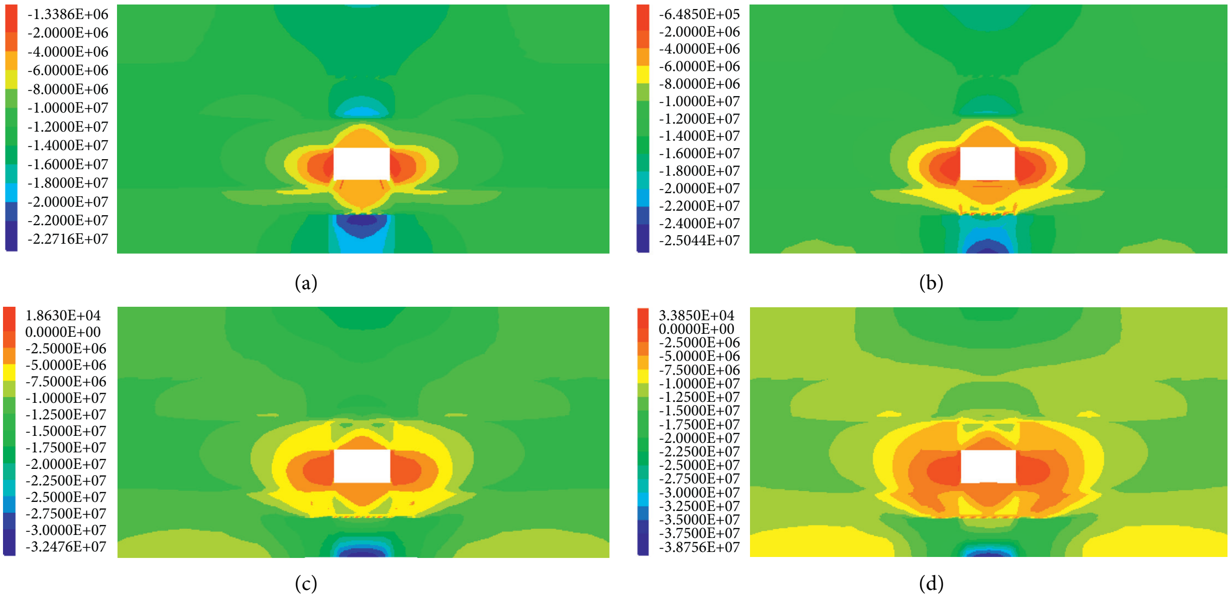

FIGURE 9: Horizontal stress cloud diagram. (a) Horizontal stress with peak stress wave of 0 MPa. (b) Horizontal stress with a peak stress wave of 5 MPa. (c) Horizontal stress with peak stress wave of 11 MPa. (d) Horizontal stress with peak stress wave of 15 MPa.

displacement in two sides. From Figure 14(a), when the loading process of stress wave starts, the roof subsidence behaviors have a maximum-minimum-stable trend. When the disturbing intensity of stress wave increases, the roof subsidence increases. In Figure 14(b), when the disturbing intensity of stress wave increases, the displacement of roof changes nonlinearly with an increasing-decreasing trend. Figures 14(c)–14(d) illustrate that the displacement changes of two sides is the same. When the intensity of the stress wave increases, the displacements of two sides increase.

Figure 15 shows the evolution of vertical displacement in the roadway roof and floor and horizontal displacement of two sides. From Figure 15(a), when the disturbing intensity of stress wave increases, the maximum, minimum, and stable values of the roof subsidence increase, and the stable value increases fastest. When the disturbing intensity of stress wave increases from 3 MPa to 15 MPa, the stable displacement in roof increases from 8.94 to 54.46 mm with an increase of 509%. The linear function of the maximum roof subsidence and the disturbing intensity of stress wave

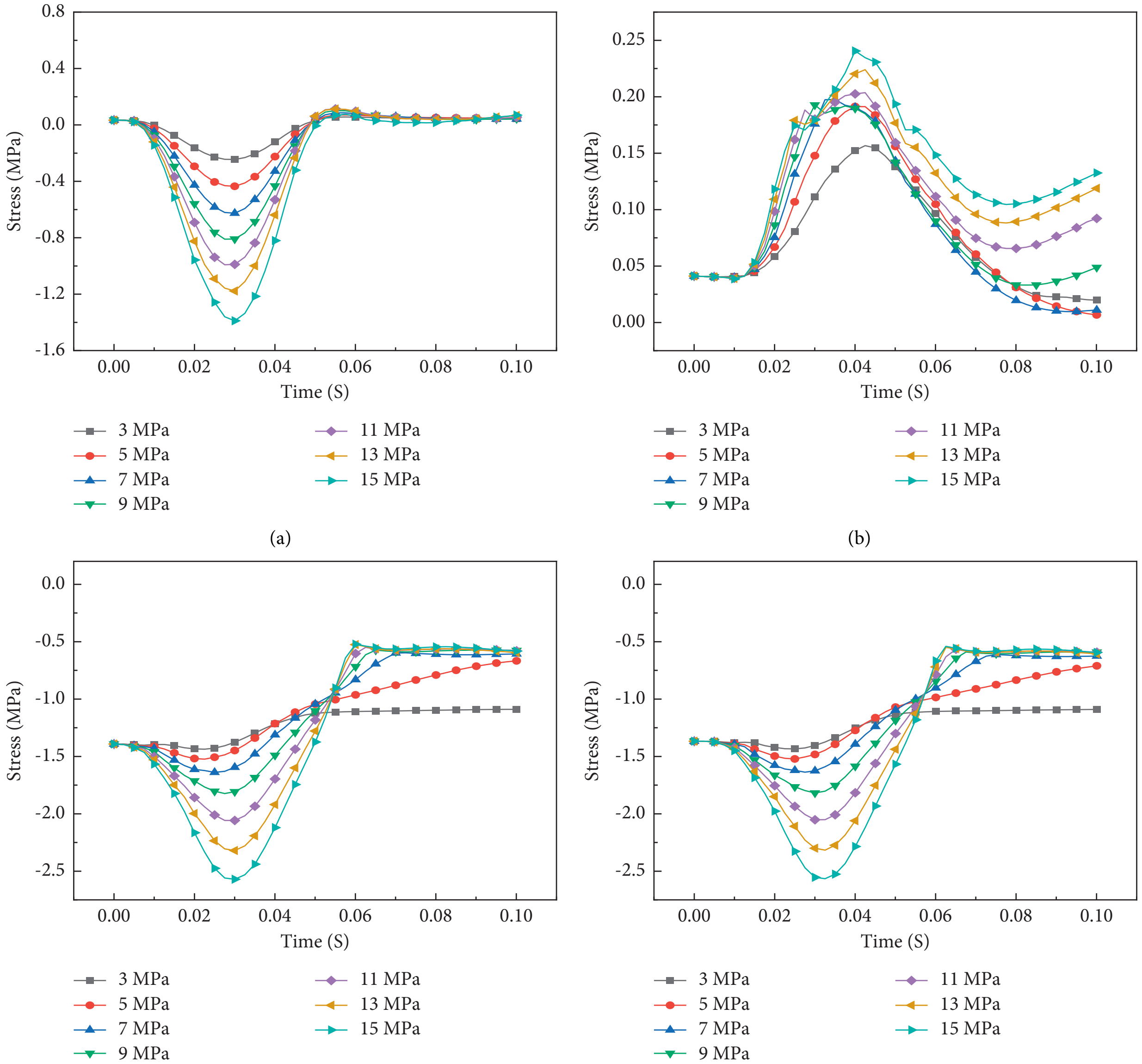

(a) (b) (c) (d)

FIGURE 10: Vertical and horizontal stress time history curves under different stress wave intensities. (a) Vertical stress time history curve of roof. (b) The vertical stress time history curve of floor. (c) The horizontal stress time history curve of the left side. (d) The horizontal stress time history curve of the right side.

disturbance is obtained by fitting. In Figure 15(b), the floor heaving exhibits a fluctuating change that first increases and then decreases. The inflection point appears when the disturbing intensity of stress wave is 5 MPa, and the maximum floor heaving decreases after the inflection point. When the disturbing intensity of stress wave increases from 3 MPa to 15 MPa, the stable floor heaving is reduced from 4.88 mm to 0.96 mm, with a reduction rate of 408%. In Figures 15(c)–15(d), the maximum, minimum, and stable displacements in two sides increase linearly, and the stable displacement has the largest increase, from 2.52 mm to 26.39 mm, with a growth rate of 947.2%. The linear function between the maximum displacement in two sides of roadway and the intensity of stress wave is shown in Figures 15(c)–15(d). Under the disturbance of stress wave, the impact loading has the greatest influence on the roadway roof.

4.3. Evolution of Plastic Zone. Figure 16 shows the plastic-failure zone of roadway surrounding rock in roof, floor, and two sides under different intensities of stress wave. The volume of plastic zone is calculated by self-compiled FISH code. In Figures 16(a)–16(d), when the disturbing intensity of stress wave increases, the failure range of roadway

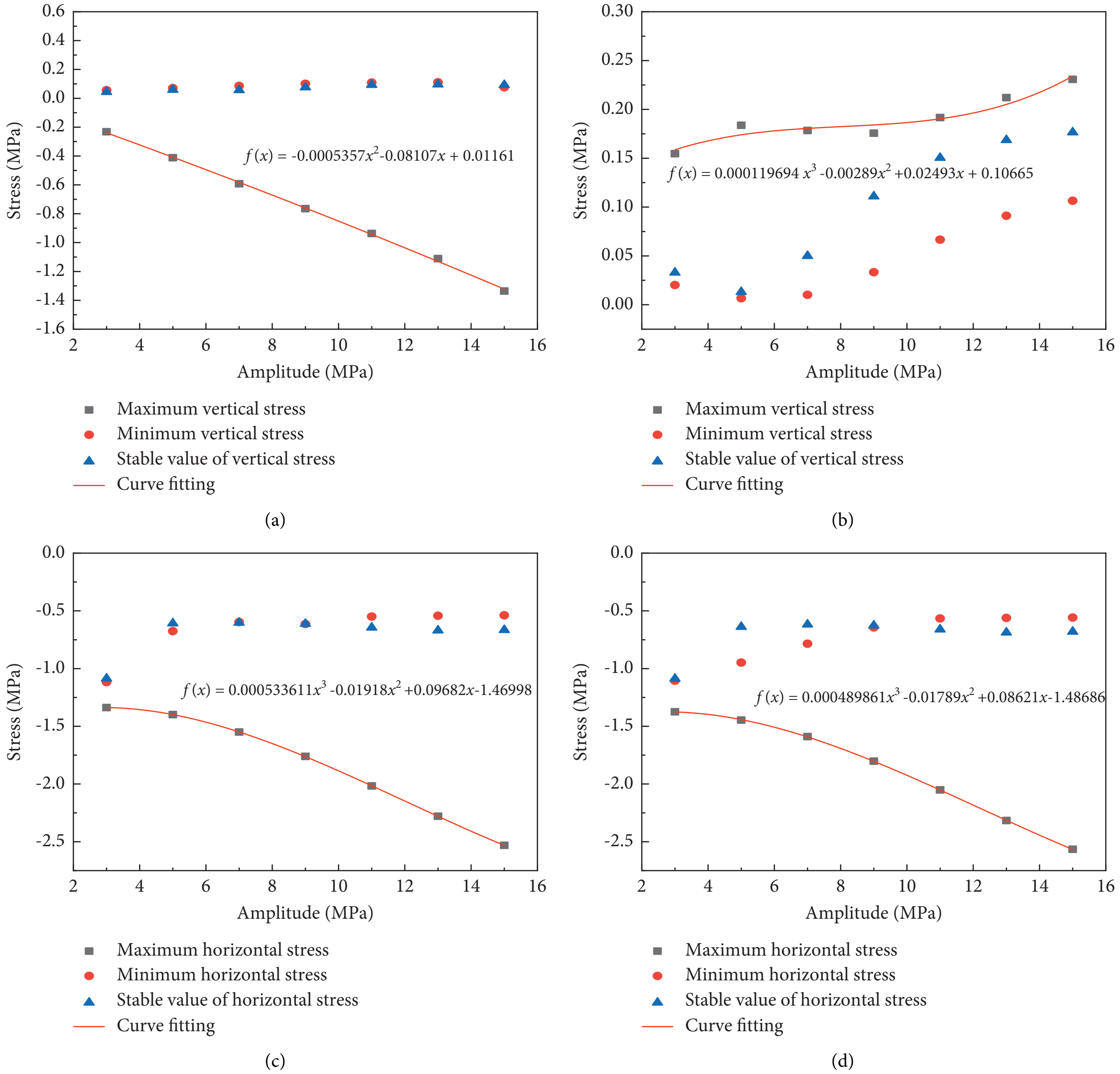

(a) (b) (c) (d)

Figure 11: Relationship between stress wave intensity and vertical and horizontal stress. Relationship between (a) vertical stress in roof and stress wave intensity, (b) vertical stress in floor and stress wave intensity, (c) horizontal stress in left side and stress wave intensity, and (d) horizontal stress in right side and stress wave intensity.

surrounding rock gradually increases as new_shear failure occurs. The shear failure range in roof increases, and the failure area shows a convex shape. The main area in floor is shear failure, and the area of tensile failure is continuously expanding. Firstly, the shear failure in two sides occurs, and then tensile failure occurs. Under the disturbing effect of stress wave, the tensile failure of surrounding rock in roof appears earlier than in the floor.

Figure 17 shows the relationship between plastic zone and disturbing intensity of stress wave in different states. In Figure 17(a), the volume shows increasing in shear_now when the peak value of stress wave increases. When the disturbing intensity of stress wave increases from 3 MPa to 15 MPa, the volume of shear failure increases from 250.37 m^3 to 795.97 m^3, and the growth rate is 218%. In Figure 17(b), the tension_now shows an increasing-decreasing-increasing trend. When the disturbing intensity of stress wave is 9 MPa, the volume of tension_now is the largest. In Figures 17(c)–17(d), when the disturbing intensity of stress wave increases, the volume of tension_now shows increasing-decreasing-increasing trend. In Figure 17(c), the volume of shear_past increases steadily. However, when the disturbing intensity of stress wave increases from 11 MPa to 13 MPa, the volume of shear_past suddenly increases from 811.27 m^3 to 1172.84 m^3, and the growth rate is 45%. In Figure 17(d), the total volume of tension_past increases steadily. When the disturbing intensity of stress wave increases from 7 MPa to 9 MPa, the volume increases suddenly

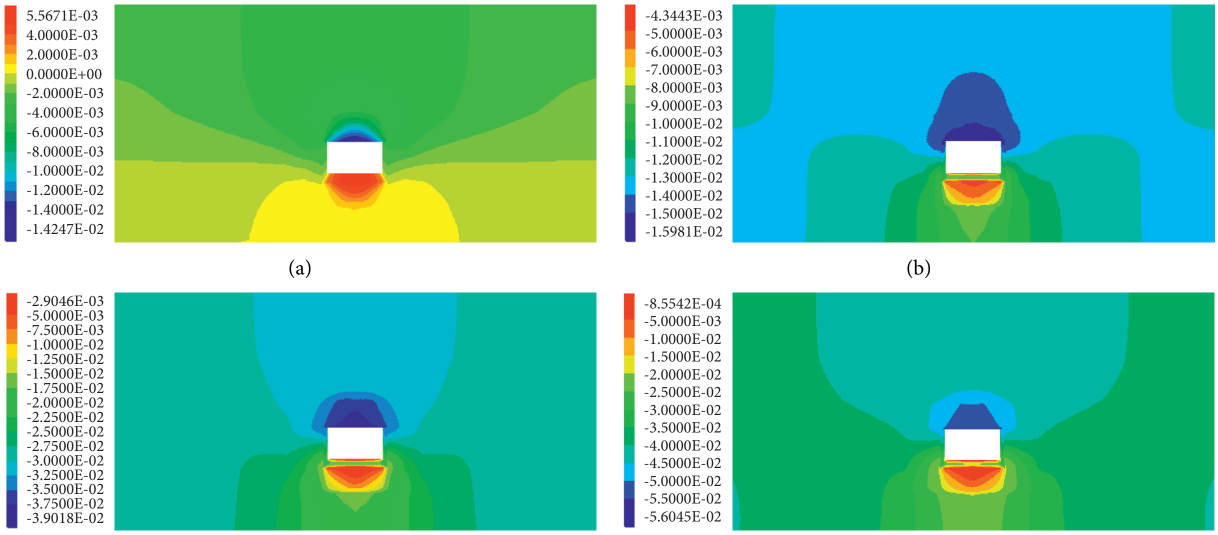

(a) (b)

(c) (d)

Figure 12: Vertical displacement contour with different peak stress waves. Vertical displacement with (a) peak stress wave of 0 MPa, (b) peak stress wave of 5 MPa, (c) peak stress wave of 11 MPa, and (d) peak stress wave of 15 MPa.

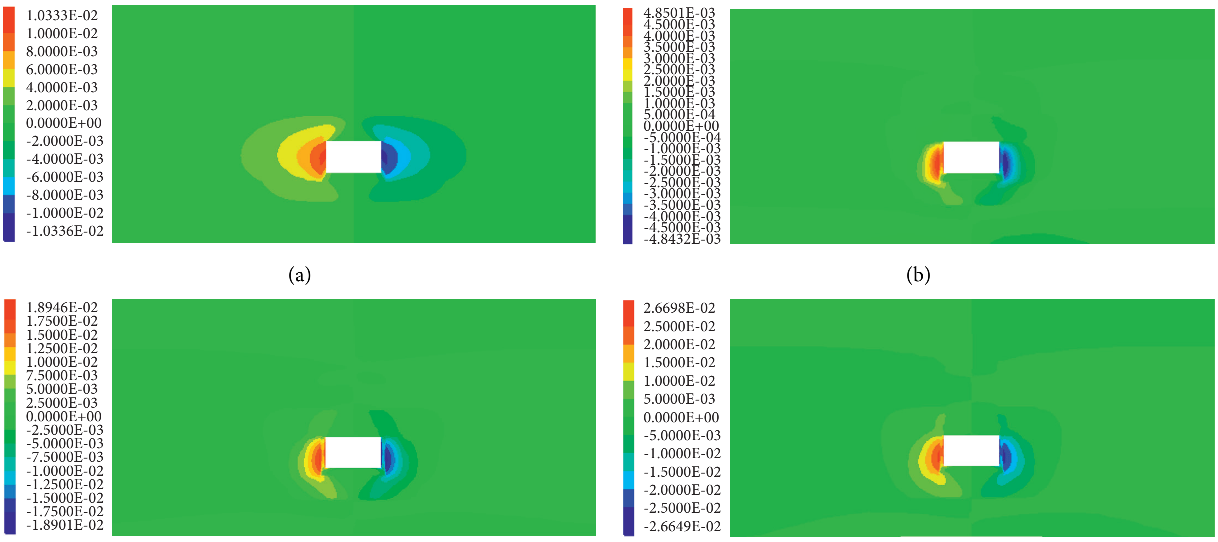

(a) (b)

(c) (d)

Figure 13: Horizontal displacement contour with different peak stress waves. Horizontal displacement with (a) peak stress wave of 0 MPa, (b) peak stress wave of 5 MPa, (c) peak stress wave of 11 MPa, and (d) peak stress wave of 15 MPa.

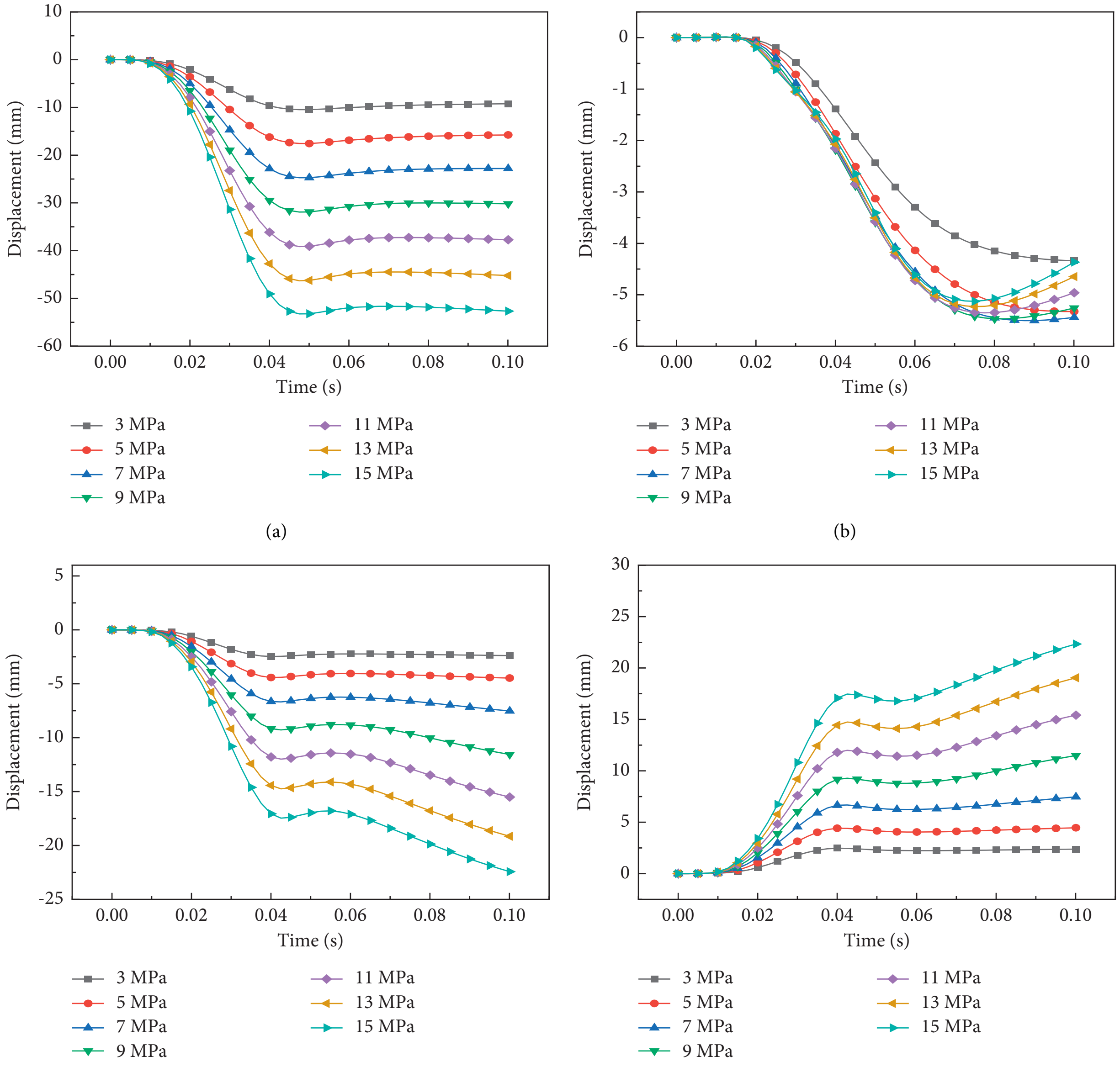

(a)

(b)

(c)

(d)

Figure 14: Displacement time history curve. Vertical displacement time history curve of the (a) roof and (b) floor. Horizontal displacement time history curve of the (c) left side and (d) right side.

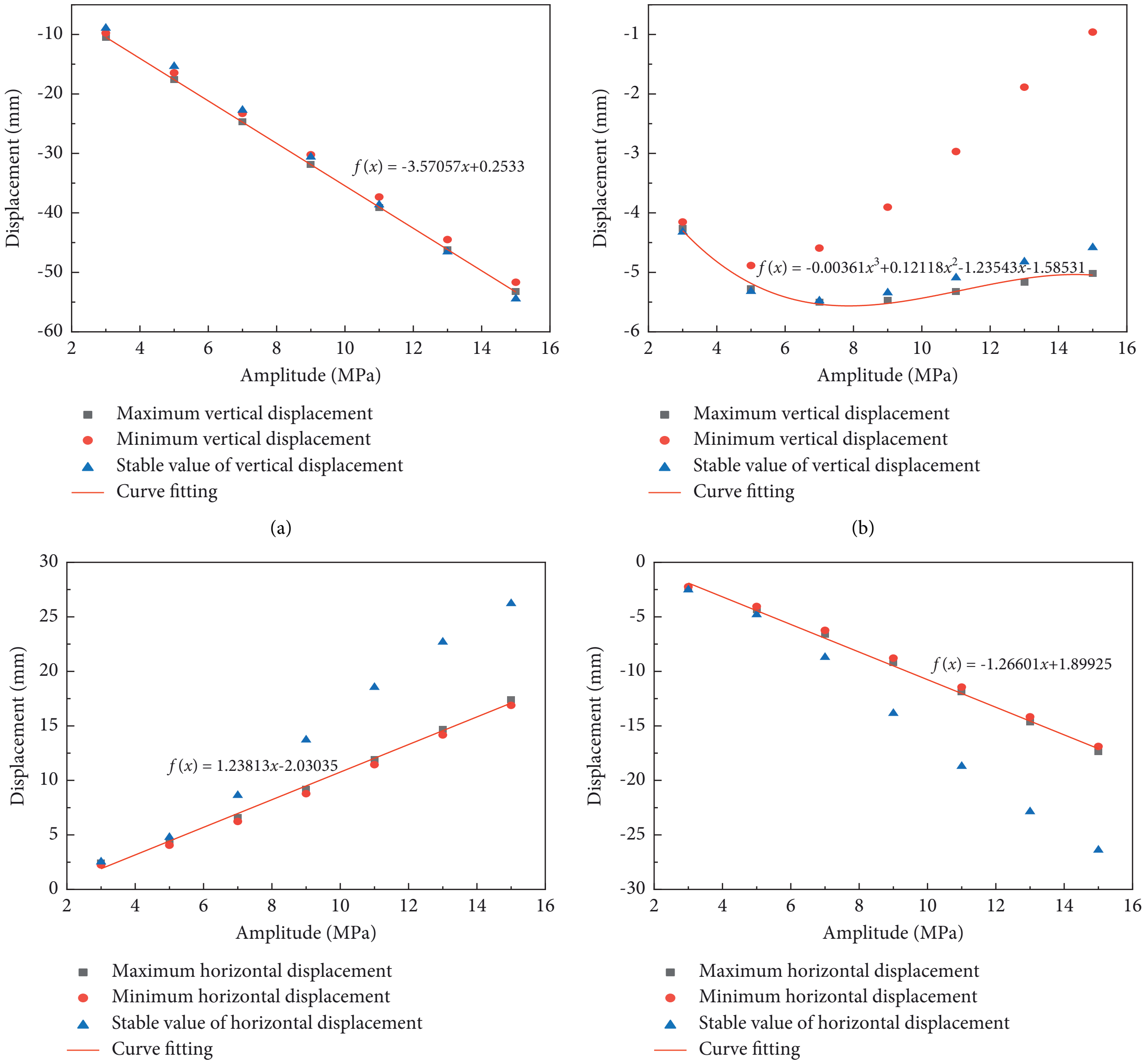

(a) (b) (c) (d)

Figure 15: Relationship between stress wave disturbing intensity and vertical and horizontal displacement. Relationship between vertical displacement in (a) roof and stress wave intensity, (b) floor and stress wave intensity, and (c) floor and stress wave intensity. Relationship between horizontal displacement in (d) left side and stress wave intensity and (e) right side and stress wave intensity.

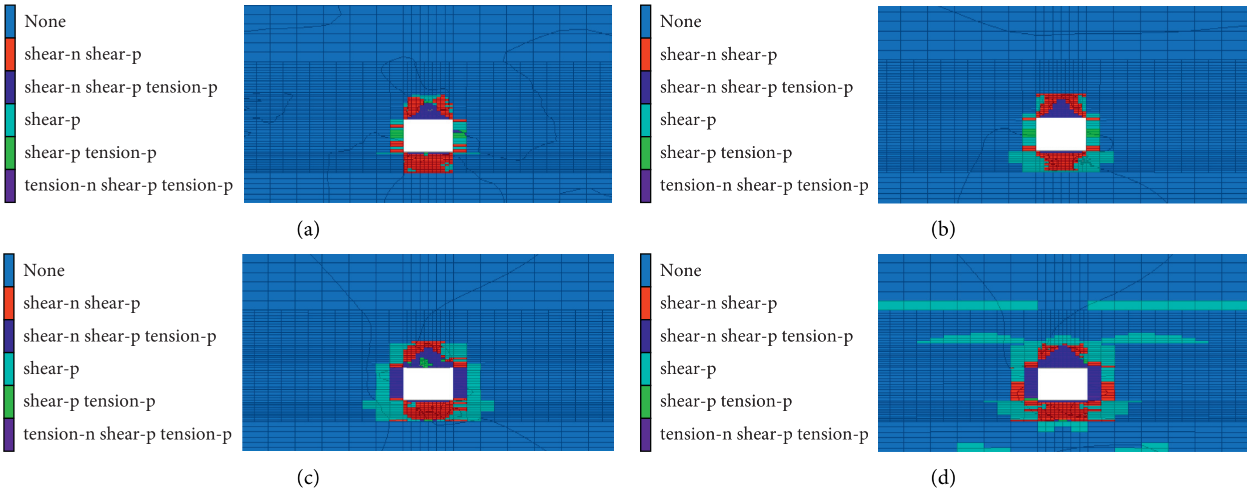

Figure 16: Plastic zone of roadway surrounding rock. Plastic zone with stress wave peak value of (a) 0 MPa, (b) 5 MPa, (c) 11 MPa, and (d) 15 MPa.

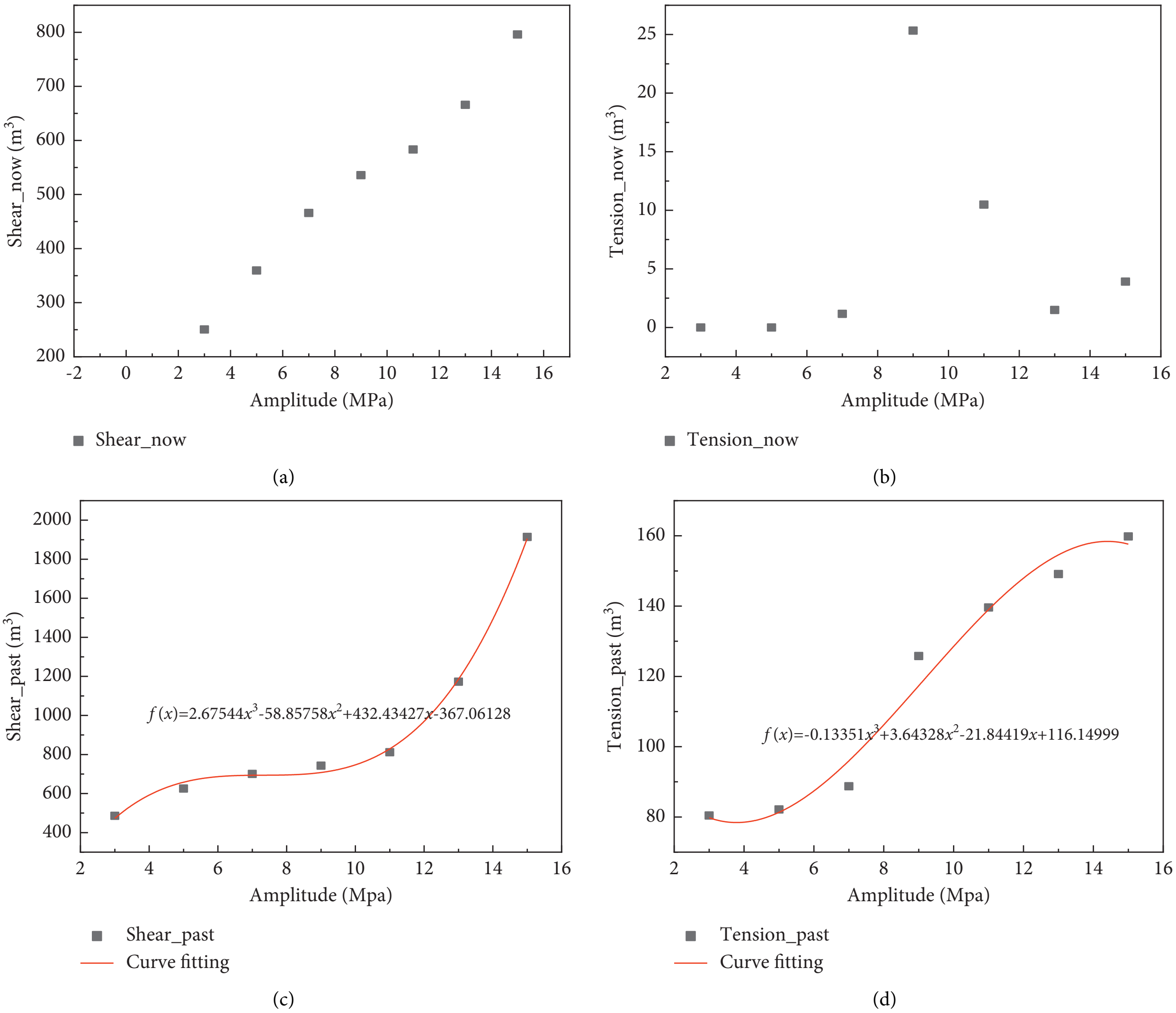

Figure 17: The volume value of the plastic zone in different states. The volume value of (a) shear_now, (b) tension_now, (c) shear_past, and (d) tension_past.

from 88.74 m^3 to 125.8 m^3, and the growth rate is 42%. The cubic interpolation polynomial functions between the volume in shear_past, tension_past, and the intensity of stress wave are shown in Figures 17(c)–17(d).

5. Conclusions

Taking the Zhangcun 2802 haulage roadway as the engineering geological background, 7 groups of numerical experiments on the mechanical characteristics of roadway surrounding rock under different stress waves are designed. The evolution law of stress, displacement, and plastic zone are contrastively analyzed and discussed. The conclusions are as follows:

(1) During the compact loading of stress wave, the stress and displacement curves in surrounding rocks of the roof, floor, and two sides show fluctuations. The maximum, minimum, and stable values appear in the fluctuation process, which is similar to the harmonics. As the peak value of stress wave disturbance increases, the resistant ability of the roof is lower than that of the floor, and the resistant ability of the two banks is the same.

(2) Self-developed FISH code can be used to solve the volume of the plastic zone in roadway surrounding rock, and thus the relationship between the plastic zone and the peak value of the stress wave disturbance under different conditions is obtained. Both of the shear_past and tension_past volumes have a third-order polynomial interpolation relationship with the disturbing intensity of stress wave. When the disturbing intensity of stress wave is 11 MPa, stress wave has the greatest influence on the increased volume of shear_past state. When the disturbing intensity of stress wave is 7 MPa, stress wave has the greatest influence on the increased volume of tension_past state.

(3) The polynomial equations between the stress within the surrounding rocks and the peak stress wave are obtained. The polynomial function equations of the displacement in the roof, floor, and two-sides are gained with good fitting effect. These results provide a reference basis for roadway surrounding rock support under impact loadings.

Data Availability

The data used in this article are from the simulation results by Flac^{3D}. The data are available from the corresponding author upon request. Experimental data used to support the findings of this study are included within the article.

Conflicts of Interest

The authors declare that there are no conflicts of interest with respect to the research, authorship, and/or publication of this article.

Acknowledgments

This research was financially supported by the National Natural Science Foundation of China (grant nos. 52174117, 52074146, and 51874159), the Natural Science Foundation of Liaoning Province (grant no. 2020-KF-13-05), and the project supported by the Postdoctoral Science Foundation of China (grant no. 2021T140290).

References

[1] X. Li, F. Gong, M. Tao et al., “Failure mechanism and coupled static-dynamic loading theory in deep hard rock mining: a review,” *Journal of Rock Mechanics and Geotechnical Engineering*, vol. 9, no. 4, pp. 767–782, 2017.

[2] G. A. Zhu, L. M. Dou, C. B. Wang, Z. W. Ding, Z. J. Feng, and F. Xue, “Experimental study of rock burst in coal samples under overstress and true-triaxial unloading through passive velocity tomography,” *Safety Science*, vol. 117, pp. 388–403, 2019.

[3] Z. L. Li, X. Q. He, L. M. Dou, D. Z. Song, G. F. Wang, and X. L. Xu, “Investigating the mechanism and prevention of coal mine dynamic disasters by using dynamic cyclic loading tests,” *Safety Science*, vol. 115, pp. 215–228, 2019.

[4] D. Xue, J. Zhou, Y. Liu, and L. Gao, “On the excavation-induced stress drop in damaged coal considering a coupled yield and failure criterion,” *International Journal of Coal Science & Technology*, vol. 7, no. 1, pp. 58–67, 2020.

[5] X. Li and F. Gong, “Research progress and prospects of deep mining rock mechanics based on combined dynamic and static loading mechanics tests,” *Journal of China Coal Society*, vol. 46, no. 3, pp. 846–866, 2021.

[6] G.-f. Wang, S.-y. Gong, L.-m. Dou, W. Cai, F. Jin, and C.-j. Fan, “Behaviour and bursting failure of roadways based on a pendulum impact test facility,” *Tunnelling and Underground Space Technology*, vol. 92, Article ID 103042, 2019.

[7] D. Guo, B. Zhou, K. Liu, R. Yang, and P. Yan, “Dynamic caustics test of blast load impact on neighboring different cross-section roadways,” *International Journal of Mining Science and Technology*, vol. 26, no. 5, pp. 803–808, 2016.

[8] J. Tang, S. Li, G. Qin et al., “Experiments on mechanical response and energy dissipation behavior of rockburst-prone coal samples under impact loading,” *Shock and Vibration*, vol. 2021, Article ID 9924456, 10 pages, 2021.

[9] X. Wu, L. Jiang, X. Xu, T. Guo, and P. Zhang, “Numerical analysis of deformation and failure characteristics of deep roadway surrounding rock under static-dynamic coupling stress,” *Journal of Central South University*, vol. 28, no. 2, pp. 543–555, 2021.

[10] C. Fan, L. Yang, G. Wang, Q. Huang, X. Fu, and H. Wen, “Investigation on coal skeleton deformation in CO2 injection enhanced CH4 drainage from underground coal seam,” *Frontiers in Earth Science*, vol. 9, Article ID 766011, 2021.

[11] N. Meng, J. Bai, Y. Chen, X. Wang, W. Wu, and B. Wu, “Stability Analysis of Roadside Backfill Body at Gob-Side Entry Retaining under Combined Static and Dynamic loading,” *Engineering Failure Analysis*, Article ID 105531, 2021.

[12] C. Fan, S. Li, M. Luo, W. Du, and Z. Yang, “Coal and gas outburst dynamic system,” *International Journal of Mining Science and Technology*, vol. 27, no. 1, pp. 49–55, 2017.

[13] X. Liu, S. Song, Y. Tan, and D. Fan, “Similar simulation study on the deformation and failure of surrounding rock of a large

section chamber group under dynamic loading," *International Journal of Mining Science and Technology*, vol. 31, 2021.

[14] L. Zhou, Z. Zhu, Y. Dong, and C. Niu, "Investigation of dynamic fracture properties of multi-crack tunnel samples under impact loads," *Theoretical and Applied Fracture Mechanics*, vol. 109, Article ID 102733, 2020.

[15] C. Gao, Z. Zhou, Z. Li, L. Li, and S. Cheng, "Peridynamics simulation of surrounding rock damage characteristics during tunnel excavation," *Tunnelling and Underground Space Technology*, vol. 97, Article ID 103289, 2020.

[16] C. Fan, S. Li, D. Elsworth, J. Han, and Z. Yang, "Experimental investigation on dynamic strength and energy dissipation characteristics of gas outburst-prone coal," *Energy Science & Engineering*, vol. 8, no. 4, pp. 1015–1028, 2020.

[17] S. Li, H. Wang, and Q. Qian, "etc. Research on on-site monitoring of zonal fracture phenomenon of surrounding rock in deep roadway," *Chinese Journal of Rock Mechanics and Engineering*, vol. 27, no. 8, pp. 1545–1553, 2008.

[18] X. Zhou and Q. Qian, "Divisional fracture mechanism of deep-buried roadways," *Chinese Journal of Rock Mechanics and Engineering*, vol. 26, no. 5, pp. 877–885, 2007.

[19] X. Li, J. Liao, G. Zhao, Z. Zhou, and Y. Zhou, "Dynamic response law of surrounding rock of high-stress roadway under dynamic disturbance," *Science and Technology Review*, vol. 30, no. 22, pp. 48–54, 2012.

[20] W. Zhu, Y. Zuo, S. Shang, and Z. Li, "Numerical simulation of instability and rupture of deep roadway triggered by dynamic disturbance," *Chinese Journal of Rock Mechanics and Engineering*, vol. 26, no. 5, pp. 915–921, 2007.

[21] D. Fan, X. Liu, Y. Tan, S. Song, J. Ning, and Q. Ma, "Numerical simulation research on response characteristics of surrounding rock for deep super-large section chamber under dynamic and static combined loading condition," *Journal of Central South University*, vol. 27, no. 12, pp. 3544–3566, 2020.

[22] J. Wang, J. Yang, F. Wu, T. Hu, and S. A. Faisal, "Analysis of fracture mechanism for surrounding rock hole based on water-filled blasting," *International Journal of Coal Science & Technology*, vol. 7, no. 4, pp. 704–713, 2020.

[23] N. Jia, C. Wu, Z. Luo, D. Shi, and C. Xie, "Analysis of nonlinear response evolution characteristics of goaf surrounding rock under dynamic disturbance," *Blasting*, vol. 33, no. 3, pp. 10–16, 2016.

[24] P. Kong, L. Jiang, and J. W. Z. Jiang, "Numerical analysis of roadway rock-burst hazard under superposed dynamic and static loads," *Energies*, vol. 12, no. 19, p. 3761, 2019.

[25] J. Xue, K. Zhan, X. Du, and Q. Ma, "Numerical simulation of the effect of dynamic stress on the rock surrounding a mine roadway," *Advances in Civil Engineering*, vol. 2020, Article ID 1656830, 10 pages, 2020.

[26] R. Zhang, G. Zhao, X. Meng et al., "Analysis on characteristics of surrounding rocks of roadway and bearing structure based on stress regulation," *Advances in Civil Engineering*, vol. 2021, Article ID 6621961, 18 pages, 2021.

[27] Q. Xu, Y. Li, J. Lu, and L. Zhang, "The use of surrounding rock loosening circle theory combined with elastic-plastic mechanics calculation method and depth learning in roadway support," *PLoS One*, vol. 15, no. 7, Article ID e0234071, 2020.

[28] M. He, F. Ren, and D. Liu, "Rockburst mechanism research and its control," *International Journal of Mining Science and Technology*, vol. 28, no. 5, pp. 829–837, 2018.

[29] W. Cai, X. Bai, G. Si, W. Cao, S. Gong, and L. Dou, "A monitoring investigation into rock burst mechanism based on the coupled theory of static and dynamic stresses," *Rock Mechanics and Rock Engineering*, vol. 53, no. 12, pp. 5451–5471, 2020.

[30] Z. Sun, L. Jiang, J. Jiang et al., "Parametric study on the ground control effects of rock bolt parameters under dynamic and static coupling loads," *Advances in Civil Engineering*, vol. 2020, Article ID 5247932, 12 pages, 2020.

[31] X. Bai, Z. Tang, T. Zhao, Z. Cheng, and K. Chen, "Microseismic response characteristics induced by mining activities: a case study," *Advances in Civil Engineering*, vol. 2021, Article ID 9977589, 18 pages, 2021.

[32] P. V. Nikolenko, S. A. Epshtein, V. L. Shkuratnik, and P. S. Anufrenkova, "Experimental study of coal fracture dynamics under the influence of cyclic freezing-thawing using shear elastic waves," *International Journal of Coal Science & Technology*, vol. 8, no. 4, pp. 562–574, 2021.

[33] ITASCA, *Fast Lagrangian Analysis of Continua its Application in 3 Dimension*, ITASCA, Minneapolis, MA, USA, 2007.